Non-Rigid Image Registration under Non-Deterministic Deformation Bounds

Qian Ge[a], Namita Lokare[a] and Edgar Lobaton[a] *

[a]Department of Electrical and Computer Engineering
North Carolina State University
Raleigh, NC 27606, USA

ABSTRACT

Image registration aims to identify the mapping between corresponding locations in an anatomic structure. Most traditional approaches solve this problem by minimizing some error metric. However, they do not quantify the uncertainty behind their estimates and the feasibility of other solutions. In this work, it is assumed that two images of the same anatomic structure are related via a Lipschitz non-rigid deformation (the registration map). An approach for identifying point correspondences with zero false-negative rate and high precision is introduced under this assumption. This methodology is then extended to registration of regions in an image which is posed as a graph matching problem with geometric constraints. The outcome of this approach is a homeomorphism with uncertainty bounds characterizing its accuracy over the entire image domain. The method is tested by applying deformation maps to the LPBA40 dataset.

Keywords: Non-rigid image registration, Lipschitz deformation, Uncertainty quantification

1. INTRODUCTION

In the medical imaging field, registration plays a very important role in the analysis of medical images for diagnosis of pathologies. There is a broad variety of medical imaging registration problems and approaches that can be categorized based on criteria such as dimensionality (2D vs. 3D), nature of registration basis, nature of transformation, optimization procedure, imaging modalities, subject and object.[1] In particular, rigid registration methods[2,3] are used when the anatomical structures are assumed to be the same up to some rigid transformation. More generally, non-rigid transformations capture more complicated deformation models. Approaches to identify these transformations include the use of mutual information,[4] fluid registration techniques,[5] and elastic models.[6]

A rigid registration method that combined intensity and gradient information for registration of 3-D ultrasound with MR images was introduced by Roche et. al.[7] To improve the robustness of rigid registration method, Ourselin et. al.[8] introduced a framework that uses a multi-scale hierarchy strategy.

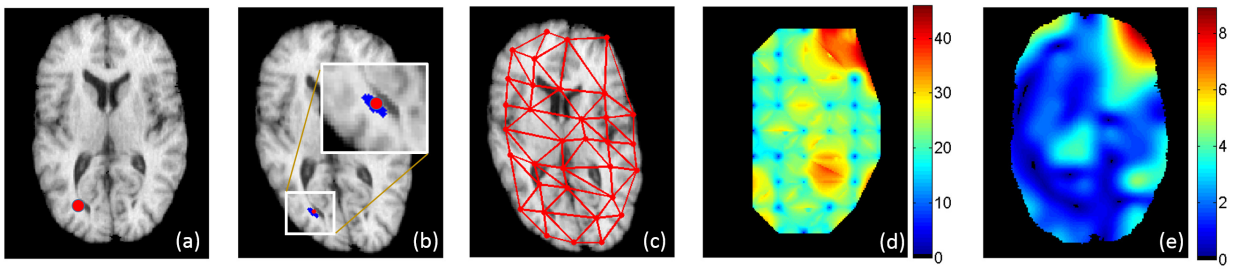

Figure 1. Registration Approach: (a) Test point x_0 (in red) on image before deformation. (b) Corresponding feasible matching set $\mathcal{S}_{x_0}$ (in blue) and true matching (in red). (c) Delaunay triangulation of selected match points. (d) Uncertainty bound in pixels (image has size 149×188). (e) Difference in pixels between truth and estimated deformation maps.

*This work was partially supported by the National Science Foundation under award CNS-1239323.
Further author information: (Send correspondence to E.L.)
Q.G.: E-mail: qge2@ncsu.edu; N.L.: E-mail: ndlokare@ncsu.edu; E.L.: E-mail: edgar.lobaton@ncsu.edu

Varied pathologies give rise to abnormal structures and the transformation required becomes highly non-linear. Non-rigid registration methods[4–6] use different approaches such as mutual information, fluid registration and elastic models to solve this problem. A statistically-assisted fluid image registration algorithm was introduced by Brun et. al.[5] which used a nonconservative Lagrangian approach. Schnabel et. al.[9] present a framework for non-rigid registration, they combined multi-resolution optimization with free form deformations. Bhatia et. al.[10] propose a groupwise, non-registration algorithm to simultaneously register all subjects in a population to a common reference that is calculated by using the gradient projection method for constrained optimization to maximize the similarity between the images.

Elastic registration methods summarized by Moghe et. al.[11] account for deformations that are elastic in nature. Klein et. al.[12] have developed "elastik", an intensity based medical image registration which could be tailored to specific applications by using suitable parametric methods. Many non-rigid registration methods use optimization to find the global minimum. Jenkinson and Smith[13] proposed a global optimization method to reliably find the global minimum to have a robust affine registration of brain images. Mark et. al.[14] focus on the optimization of the intensity-based cost function to reduce the mis-registration due to getting trapped in local minima. Most of these methods mentioned above do not quantify their uncertainty.

In this paper we propose a new non-rigid markerless registration method based on point matching under the assumption that two images are related via a Lipschitz non-rigid transformation. This approach is tested on 2D images but is also applicable to 3D. Sets of feasible matching points are obtained by constructing a functional descriptor that guarantees the inclusion of the correct matching point under the specified deformation bounds. Image registration is performed by incorporating these feasible sets into a graph matching problem with geometric constraints. Finally, uncertainty bounds due to the size of the feasible matching sets are combined to generate bounds on the estimated map. Fig. 1 illustrates a result based on our approach. The rest of the paper is organized as follows: section 2 describes our method, section 3 presents our experimental results, and section 4 provides some final remarks.

2. METHOD

2.1 Image Model

We assume that two images ($I_k : \Omega_k \to \mathbb{R}$ where $k \in \{0,1\}$ and $\Omega_k \subset \mathbb{R}^2$) are related by:

$$I_1 \circ f_{10}(x) = I_0(x) \tag{1}$$

where $f_{10} : \Omega_0 \to \Omega_1$ is a homeomorphism (with inverse f_{01}) that satisfies:

$$(1 - K_d)\|f_{10}(x) - f_{10}(y)\| \leq \|x - y\| \leq (1 + K_d)\|f_{10}(x) - f_{10}(y)\|. \tag{2}$$

for all $x, y \in \Omega_0$, where K_d is a factor bounding the unknown deformation. Throughout the rest of the paper, we assume that the constant K_d is known but the actual deformation mappings f_{10} and f_{01} are unknown.

2.2 Robust Pre-Processing

Before attempting to extract any descriptors, images are pre-processed in a way that guarantees the descriptors will be robust to the unknown deformation, noise, and the discretization process. Images are filtered by first computing the cumulative distribution $F_{k,B(x,r)} : \mathbb{R} \to [0,1]$ of values of image I_k, $k \in \{0,1\}$, over a neighborhood $B(x,r)$, where $B(x,r)$ is the ball with radius r centered at x. That is,

$$F_{k,B(x,r)}(s) = \frac{1}{\pi r^2} \int_{B(x,r)} \mathbb{1}_{I_k^{-1}(-\infty,s]}(y)dy \quad \text{for} \quad k \in \{0,1\}, \tag{3}$$

where $\mathbb{1}_A(\cdot)$ is the indicator function for set A. This function indicates the fraction of points in $B(x,r)$ that have intensity values below s. The **pre-processed images** are defined as:

$$\begin{array}{lll} J_{0-}(x) = F^{-1}_{0,B(x,(1+K_d)\rho)}(\tau_-), & J_0(x) = F^{-1}_{0,B(x,\rho)}(\tau), & J_{0+}(x) = F^{-1}_{0,B(x,(1+K_d)\rho)}(\tau_+), \\ J_{1-}(x) = F^{-1}_{1,B(x,(1-K_d)^{-1}\rho)}(\tau_-), & J_1(x) = F^{-1}_{1,B(x,\rho)}(\tau), & J_{1+}(x) = F^{-1}_{1,B(x,(1-K_d)^{-1}\rho)}(\tau_+) \end{array} \tag{4}$$

where

$$\tau_- = \left(\frac{1-K_d}{1+K_d}\right)^2 \tau \quad , \quad \tau_+ = 1 + \left(\frac{1-K_d}{1+K_d}\right)^2 (\tau - 1), \tag{5}$$

ρ indicates the size of the neighborhood used for filtering. By choosing $\tau = 0.5$, then J_k is the outcome of applying a median filter to I_k, which has well-known robustness properties. When $K_d = 0.2$, $\tau_- = 0.22$ and $\tau_+ = 0.78$. J_{k-} and J_{k+} are similar to the outcome of applying dilation and erosion to I_k. Fig. 2 (left) shows some pre-processed images for two deformed images.

THEOREM 2.1. *Given the above definitions, for all $\rho > 0$,*

$$J_{k-}(x) \leq J_{(1-k)} \circ f_{(1-k)\,k}(x) \leq J_{k+}(x) \quad \textit{for} \quad k \in \{0, 1\}. \tag{6}$$

This theorem is essential for the development of the robust descriptors that are introduced in the next section. The parameter ρ is selected to be large enough to perform a robust filtering that removes effects due to discretization and noise, which maintains Theorem 2.1. Experiments indicate that a value of $\rho = 2$ is sufficient for most applications. Larger value of ρ produces more robustness to discretization and noise, but yields larger potential matching set. Note that when $\rho \to \infty$, the filtered images are constant images and all the points in I_1 will be potential matching points to points in I_0.

Note that this filtering does not require exact knowledge of the image mapping f_{10} and f_{01}, but instead makes use of the provided bounds.

2.3 Robust Functional Image Descriptor

In order to characterize a region around a point, a function is extracted to describe how color intensity changes as a function of distance. The **localized upper kernel function** is defined as

$$D^U_\alpha(x, z|R) = \inf_{x^*}\{\|x^* - x\| \big| x^* \in J^{-1}_\alpha[z, \infty) \cap B(x, R)\} \tag{7}$$

where $\alpha \in \{0-, 0, 0+, 1-, 1, 1+\}$ and the radius R specifies the support of the descriptor, which is a ball with radius R around point x. Note that this ball is not the same ball used in pre-processing. This function captures the minimum distance between point x and points with intensity value greater or equal to z within the ball $B(x, R)$, which can be computed by taking the distance transform of the sets $J^{-1}_\alpha[z, \infty)$. When the intensity of all points within the ball is less than z, then $D^U_\alpha(x, z|R) = R$.

THEOREM 2.2. *Given a point $x_0 \in \Omega_0$ with corresponding matching point $x_1 = f_{10}(x_0) \in \Omega_1$ and a radius R, the localized upper kernel function satisfies:*

$$\begin{array}{rcl} (1+K_d)^{-1} D^U_{0+}(x_0, z|R) \leq D^U_1(x_1, z|R_{1L}) & , & D^U_1(x_1, z|R_{1U}) \leq (1-K_d)^{-1} D^U_{0-}(x_0, z|R), \\ (1-K_d) D^U_{1+}(x_1, z|R) \leq D^U_0(x_0, z|R_{0L}) & , & D^U_0(x_0, z|R_{0U}) \leq (1+K_d) D^U_{1-}(x_1, z|R) \end{array} \tag{8}$$

for all test intensity value z, where $R_{1L} = (1+K_d)^{-1}R$, $R_{1U} = (1-K_d)^{-1}R$, $R_{0L} = (1-K_d)R$ and $R_{0U} = (1+K_d)R$. Given that $\mathcal{S}^U_{x_0} \subset \Omega_1$ is the set of points that satisfy these conditions, then $x_1 \in \mathcal{S}^U_{x_0}$.

This theorem is a criteria for determining potential matching points. That is, it gives conditions between the functional descriptors that need to be satisfied for corresponding matching point. $\mathcal{S}^U_{x_0} \subset I_1$ can be obtained by checking these conditions between functional descriptors for $x_0 \in I_0$ and functional descriptors for all points in I_1.

Similar to localized upper kernel function, we define **localized lower kernel function** as

$$D^L_\alpha(x, z|R) = \inf_{x^*}\{\|x^* - x\| \big| x^* \in J^{-1}_\alpha(-\infty, z] \cap B(x, R)\} \tag{9}$$

where $\alpha \in \{0-, 0, 0+, 1-, 1, 1+\}$. Also, we have the theorem below:

THEOREM 2.3. *Given a point $x_0 \in \Omega_0$ with corresponding matching point $x_1 = f_{10}(x_0) \in \Omega_1$ and a radius R, the localized lower kernel function satisfies:*

$$\begin{array}{rcl} (1+K_d)^{-1} D^L_{0-}(x_0, z|R) \leq D^L_1(x_1, z|R_{1L}) & , & D^L_1(x_1, z|R_{1U}) \leq (1-K_d)^{-1} D^L_{0+}(x_0, z|R), \\ (1-K_d) D^L_{1-}(x_1, z|R) \leq D^L_0(x_0, z|R_{0L}) & , & D^L_0(x_0, z|R_{0U}) \leq (1+K_d) D^L_{1+}(x_1, z|R) \end{array} \tag{10}$$

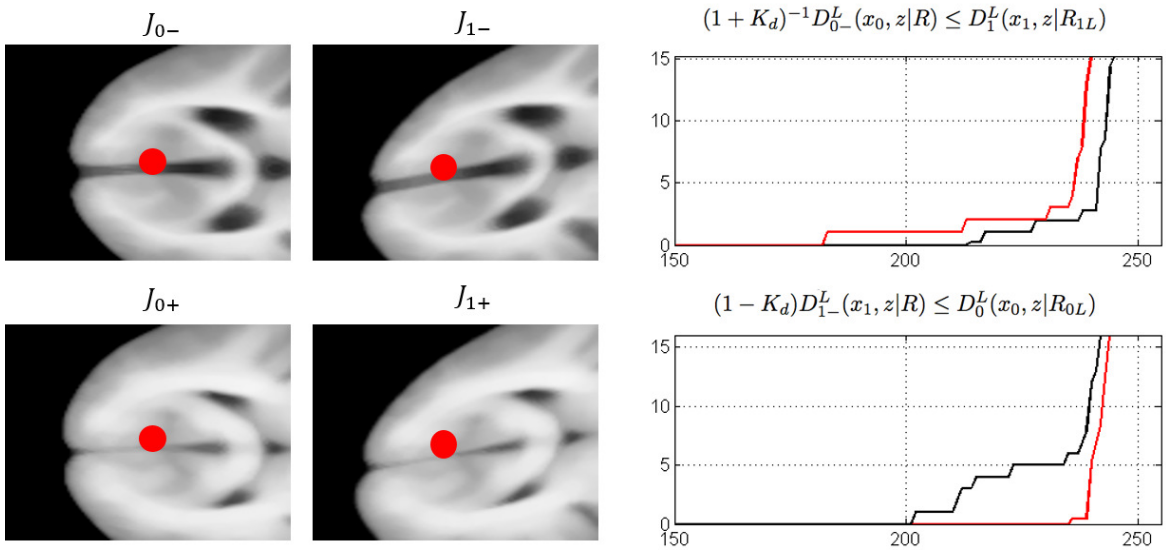

Figure 2. Functional Descriptors and Conditions for Matching. A set of pre-processed images are shown for base image I_0 (first column) and test image I_1 (second column). From top to bottom, we observe J_{k-} and J_{k+}. First and third conditions in Equation 8 on localized upper kernel function stated in Theorem 2.2 are illustrated (right plots). Functions in black are associated with I_0 and functions in red are associated with I_1. The range of z is $[0, 255]$, but only $z \in [150, 255]$ is shown. In this case, all the four functions are equal to 0 for $z \leq 150$. Note that the ordering between functions is satisfied as stated by the theorem.

for all test intensity value z. Given that $\mathcal{S}^L_{x_0} \subset \Omega_1$ is the set of points that satisfy these conditions, then $x_1 \in \mathcal{S}^L_{x_0}$.

The set $\mathcal{S}_{x_0} = \{x \big| x \in \mathcal{S}^U_{x_0} \cap \mathcal{S}^L_{x_0}\} \subset \Omega_1$ is referred to as the potential matching set for $x_0 \in \Omega_0$ where $x_1 = f_{10}(x_0) \in \mathcal{S}_{x_0}$. Fig. 2 (right) illustrates condition 8 for one matching pair and Fig. 3 shows an example of single point matching using this criteria.

2.4 Deformation Map Estimation

As introduced above, the matching result of one point is a potential matching set that guarantees the inclusion of the correct matching point, but the accurate position of the correct matching point is still unknown. A smaller potential matching set is required to estimate the position of correct matches more accurately. To achieve this, we extend our criteria for single point matching to region registration by considering a set of points $P_0 := \{x_{0,i}\} \in \Omega_0$ and computing their potential matching sets $\mathcal{S}_{x_{0,i}}$. These points are connected to each other using edges from

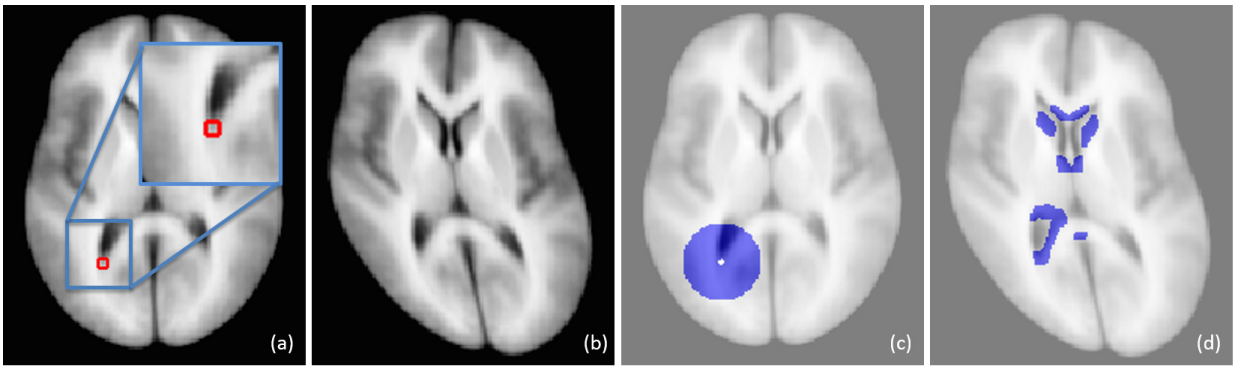

Figure 3. Single Point Matching ($K_d = 0.2$): (a) Test point (in red square). (b) Deformation image with maximum 20% deformation. (c) Support region of the descriptor (blue circle with radius 20 pixels). (d) Potential matching set (in blue) for this test point.

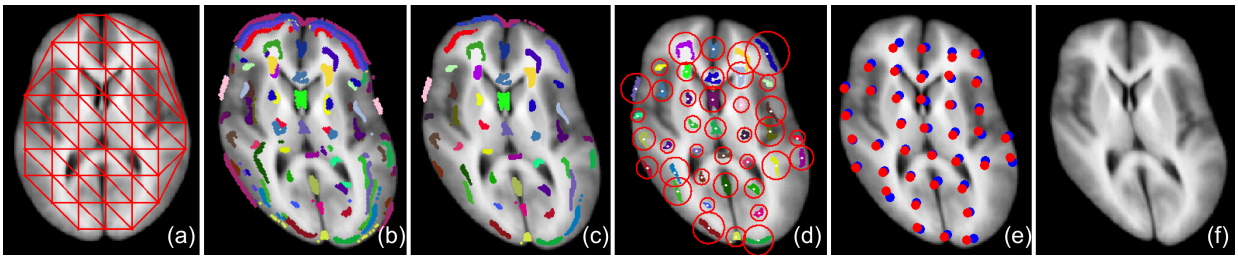

Figure 4. Map Estimation: (a) Test set P_0 and Delaunay triangulation. (b) Potential matching sets $\mathcal{S}_{x_{0,i}}$ for set P_0. Different colors denote different test points in P_0. (c) Potential matching sets $S'_{x_{0,i}}$ for set P_0 after applying distance constraint. (d) Potential matching sets $S'_{x_{0,i}}$ for set P'_0 and the minimum circle covering each $S'_{x_{0,i}}$ with radius less than γ. (e) Estimated matching points (in red) and groundtruth (in blue) for set P'_0. (f) Estimated deformation image.

their Delaunay triangulation.[15] Some wrong matches in potential matching sets can be removed by applying a geometry constraint. Also some test points in P_0 will be removed by the size of their potential matching sets.

We note that given points $x_0, y_0 \in \Omega_0$, then from formula 2, we have

$$(1 + K_d)^{-1}\|x_0 - y_0\| \leq \|f_{10}(x_0) - f_{10}(y_0)\| \leq (1 - K_d)^{-1}\|x_0 - y_0\|. \tag{11}$$

The above result can be used to determine the feasibility of a point $x_{1,i} \in \mathcal{S}_{x_{0,i}}$ by checking if the condition is satisfied by any point $x_{1,j} \in \mathcal{S}_{x_{0,j}}$, where $x_{0,i}$ and $x_{0,j}$ are connected by an edge. If not, then the point $x_{1,i}$ is an unfeasible matching point and removed from $\mathcal{S}_{x_{0,i}}$. The remaining sets are still guaranteed to contain the correct matching points, since the correct matches will always satisfy condition 11.

To be more accurate, the set P_0 is refined by selecting only those points that have a "small" matching set. This is done by making sure that $\mathcal{S}_{x_{0,i}}$ is connected, and all the points in matching set are within a distance γ from its center of mass. Let the remaining set be P'_0 and the corresponding matching points are estimated by the center of each remaining matching set $S'_{x_{0,i}}$. Finally, the estimated homeomorphism $\hat{f}_{10}$ and $\hat{f}_{01}$ is obtained using Radial basis Functions.[16] The estimated deformed image is obtained by $\hat{I}_1(x) = I_0 \circ \hat{f}_{01}(x)$. Fig. 4 shows the process of deformation map estimation.

2.5 Uncertainty Computation

Statistical analysis of brain images (e.g. detection of lesions in the brain) often relies on the extraction of correlation information at certain voxel locations. It is often assumed that the registration images are properly aligned, which can introduce some bias on the statistical models. However, if a bound on uncertainty on the registration map was provided, this could be built into the modeling tools leading to more accurate statistical models. In this section, we will introduce a way to determine the uncertainty of the estimation map.

First we define the feasible region $V \subset \Omega_1$ for a point $x_0 \in \Omega_0$ that is a collection of the possible positions of correct match for x_0. Let $\hat{x}_1 \in \Omega_1$ be the estimated matching point for x_0, then the uncertainty of x_0 is defined as

$$U = \max_x \{\|x - \hat{x}_1\| \big| x \in V\}. \tag{12}$$

A new Delaunay triangulation is obtained for the set P'_0 and we only consider the points within these triangles. For point $x_{0,i} \in P'_0$, the correct match can be any point in its matching set which is exactly the feasible region of $x_{0,i}$. Then the uncertainty of those points is defined as

$$U_i = \max_x \{\|x - \hat{x}_{1,i}\| \big| x \in S'_{x_{0,i}}\}, \tag{13}$$

where $\hat{x}_{1,i} \in \Omega_1$ is the estimated matching point for $x_{0,i}$. Note that the uncertainty for the points in P'_0 is less than γ by design.

The uncertainty for the points in P'_0 and the Lipschitz bound on the deformation are used to specify uncertainty within each triangle of the Delaunay triangulation. For those points, the feasible region is obtained from

the intersection of feasible regions with respect to each point in P_0'. According to formula 2, the feasible region of a point $x_0 \notin P_0'$ with respect to point $x_{0,i} \in P_0'$ is

$$V^i = \{x \big| (1+K_d)^{-1}(\|x_{0,i} - x_0\| - U_i) \leq \|\hat{x}_{1,i} - x\| \leq (1-K_d)^{-1}(\|x_{0,i} - x_0\| + U_i), x \in \Omega_1\}, \tag{14}$$

where $\hat{x}_{1,i}$ is the estimated matching point for $x_{0,i}$ and U_i is the corresponding uncertainty. To reduce the complexity, for $x_0 \notin P_0'$ in a triangle, we only consider three corresponding vertices to compute its feasible region. That is,

$$V = \cap_{i=1}^{3} V^i, \tag{15}$$

and its uncertainty is

$$U = \max_x \{\|x - \hat{x}_1\| \big| x \in V\}, \tag{16}$$

where $\hat{x}_1 = \hat{f}_{10}(x_0)$ is the estimated matching point of x_0. Note that the uncertainty of these points are determined by the size of triangle and the uncertainty of its vertices.

Fig. 1 (c) and (d) illustrate one example of new Delaunay triangulation for set P_0' and the map uncertainty. From (c), we can see uncertainty for points in P_0' is small, but it is larger for other points. The upper left part has the highest uncertainty because the triangle is large and the uncertainty for the upper leftmost point in P_0' is high.

3. RESULTS

We perform our analysis on the MRIs of 40 brains from the LPBA40 dataset[†] with size 240×270 (after some zero-padding). We selected the 80-th transverse slice. We apply 10% and 20% deformations to the original images. The deformation we consider is:

$$f_{01}\begin{pmatrix} z_1 \\ z_2 \end{pmatrix} = \begin{pmatrix} z_1 + 0.5c\ \cos(0.02 z_2) \\ z_2 + 0.5c\ \cos(0.02 z_1) \end{pmatrix} \tag{17}$$

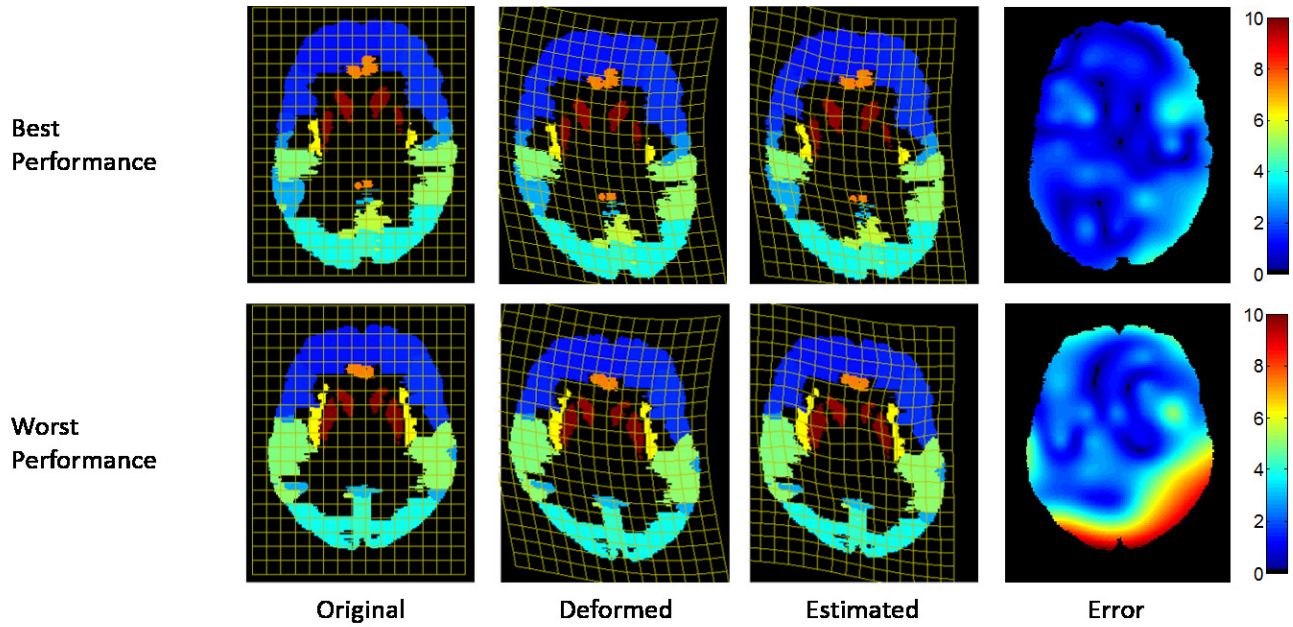

Figure 5. Results of proposed method on the labeled LPBA40 dataset with 20% deformation. Best performance (row 1) and worst performance (row 2) results are shown. Original image (1st column), deformed image (2nd column), original image transformed by estimated deformation using our method (3rd column), and error on deformation map (4th column).

[†] http://www.loni.usc.edu/atlases/

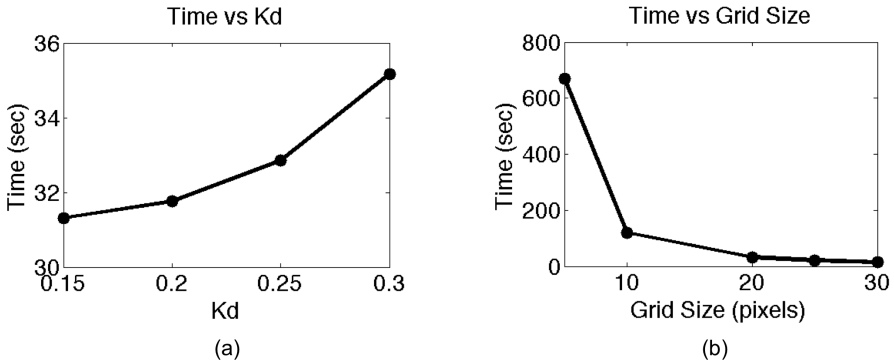

Figure 6. (a) Average time cost as a function of deformation constant K_d applied to 10% deformation images. (b) Average time cost as a function of grid size applied to 20% deformation images.

where c specifies a maximum deformation factor (e.g., $c = 10$ indicates a maximum deformation of 10%). The test points P_0 are selected to come from a uniform grid, ρ is select to be 3 and $R = 20$. The registration process, which has the single point matching implemented in C++ and the graph matching in MATLAB, is applied in a 3.4 GHz computer with 16GB RAM.

In order to evaluate our method we use three metrics: Mapping Error (ME), Target Overlap Score (TOS), and Volume Similarity Coefficient (VSC).[17] Mapping Error measures the average difference between the truth and estimated maps. It is defined as

$$ME = \frac{1}{|\Omega_0|} \int_{\Omega_0} ||f_{10}(x) - \hat{f}_{10}(x)||_2 \, dx \tag{18}$$

where $|\Omega_0|$ is the area of Ω_0, f_{10} is the true map and $\hat{f}_{10}$ is the estimated map.

For TOS and VSC, we consider the brain segmentation available in the dataset. These metrics quantify the amount of overlap between the regions obtained by using the true and estimated deformations. We only consider regions of size greater than 50 pixels for our analysis in order to avoid large overlap discrepancies due to small offsets. Samples are shown in Fig. 5. The metrics are defined as

$$TOS = \frac{\sum_r |\mathcal{R}_r \cap \hat{\mathcal{R}}_r|}{\sum_r |\mathcal{R}_r|} \qquad \text{and} \qquad VSC = 2\,\frac{\sum_r (|\mathcal{R}_r - \hat{\mathcal{R}}_r|)}{\sum_r (|\mathcal{R}_r| + |\hat{\mathcal{R}}_r|)}, \tag{19}$$

where $\mathcal{R}_r$ and $\hat{\mathcal{R}}_r$ denote the $r-$th true and estimated region in the brain respectively. For VSC, smaller values denote better registration.

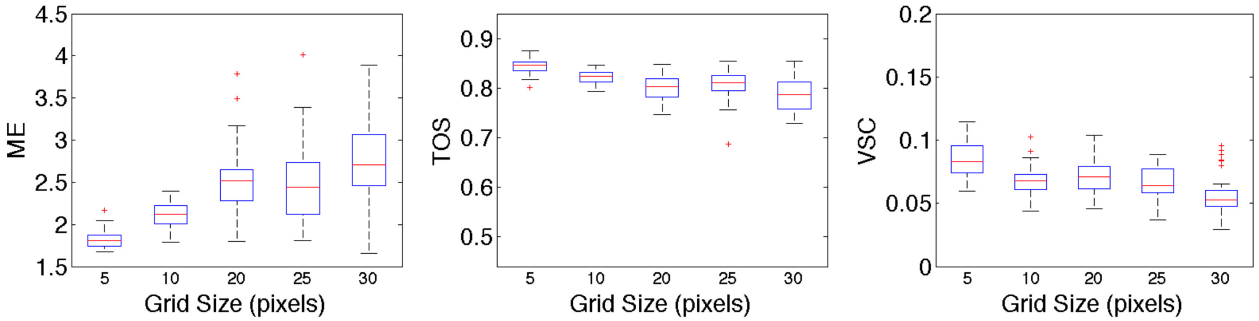

Figure 7. Box plots of evaluation results of proposed method for Mapping Error (left), Target Overlap Score (middle) and Volume Similarity Coefficient (right) metrics applied to the LPBA40 dataset for 20% deformation using uniform grid with 5, 10, 20, 25 and 30 pixels between points as test points.

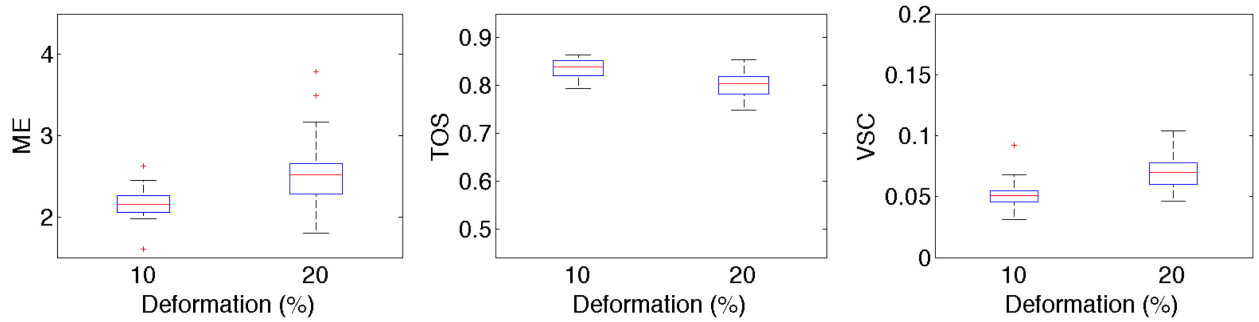

Figure 8. Box plots of evaluation results of proposed method for Mapping Error (left), Target Overlap Score (middle) and Volume Similarity Coefficient (right) metrics applied to the LPBA40 dataset with 10% and 20% deformation.

Fig. 6 and 7 show the average time cost and evaluation for 40 images in LPBA40 dataset using the proposed method. Fig. 6 (a) is the average time cost for 10% deformation using deformation constant $K_d = 0.15,\ 0.2,\ 0.25$ and 0.3. Fig. 6 (b) is the time cost for 20% deformation using uniform grid with 5, 10, 20, 25 and 30 pixels between points in the test point set. Fig. 7 shows the results for the three metrics applied to the 20% deformation with grid size 5, 10, 20, 25 and 30 pixels. Time cost increases as K_d increases, since larger K_d yields larger potential matching sets for each test point, which gives more points to be checked for feasibility. But when K_d is in the range of [0.15 0.3], it does not change too much. For grid size, smaller grid sizes, which means larger number of test points, take more time since more computation is required for points matching and graph matching. Grid size 5 which has around 800 test points takes about 700 seconds, and grid size 10 with around 200 test points takes about 120 seconds. When the grid size is greater than 20, which has less than 50 test points, it takes less than 30 seconds. From Fig. 7, the performance of different grid size does not change a lot. Grid size 5 has the best mapping error and target overlap score. The volume similarity cofficient values are relatively small and do not vary a lot with grid sizes. Grid size 30 has the best volume similarity coefficient, but the worst mapping error and target overlap score. Grid size 10, 20 and 25 have good performance for all of three metrics, but grid size 10 is time consuming as shown in Fig. 6 (b). Thus, grid size 20 and 25 are proper choices. In the following experiments, we choose uniform grid with 20 pixels between points as test point set P_0.

Fig. 8 summarizes the results for the three metrics applied to the LPBA40 dataset with 10% and 20% deformation. It is observed that the average difference between truth and estimated map is less than 2.6 pixels for both 10% and 20% deformation, which corresponds to less than 2% of the image length.

Fig. 5 shows the best and worst results of our method, with respect to the target overlap score, for a 20% deformation. In the best case, the maximum difference between the truth and estimated deformation is less than 4 pixels. For the worst case, it is less than 10 pixels. This large error is due to homogeneity in the imaging data which leads to large feasible matching sets and estimated matching points that are far away from the true values.

We compare the proposed method with the fluid registration method, SAFIRA[5] and run experiments to

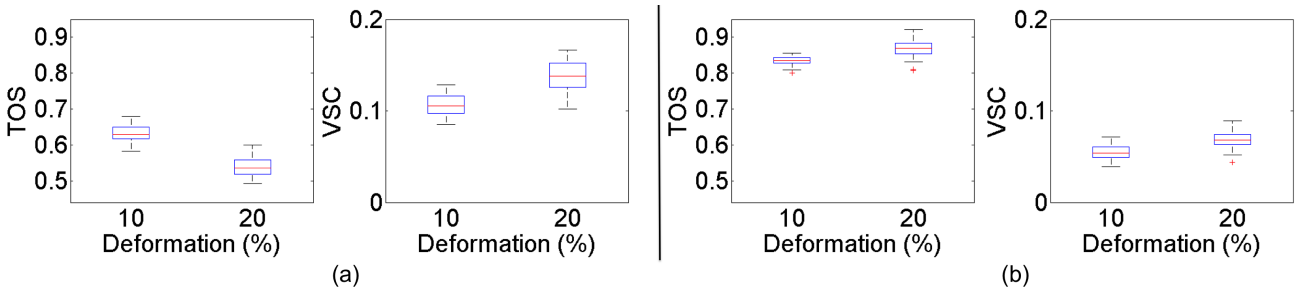

Figure 9. (a) Box plots of evaluation results of SAFIRA[5] (40 iterations) for TOS (left) and VSC (right) applied to the LBPA40 dataset with 10% and 20% deformation. (b) Box plots of evaluation results of SAFIRA[5] (40 iterations) with initialization by proposed method for TOS (left) and VSC (right) applied to the LBPA40 dataset with 10% and 20% deformation.

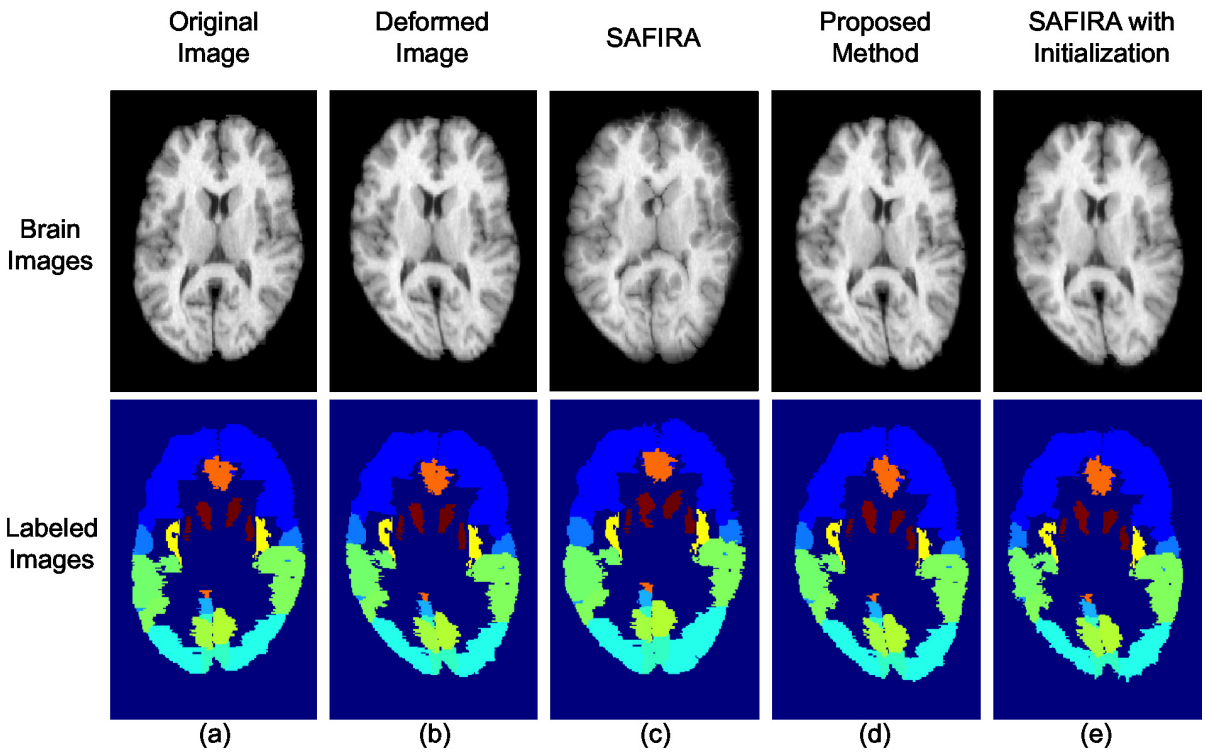

Figure 10. Sample result of images (first row) and corresponding labeled images (second row). (a) Original image. (b) 20% deformation image. (c) Result of SAFIRA[5] with $pixel\_max = 0.33$ and 40 iterations. (d) Result of proposed method with $\rho = 3$, $R = 20$, $K_d = 0.2$ and $gridsize = 20$. (e) Result of SAFIRA ($pixel\_max = 0.33$ and 40 iterations) with initialization by proposed method.

see how initialization by the proposed method improves SAFIRA performance. Overall, the proposed method performed better than SAFIRA without any initialization, and applying SAFIRA to refine our results improves performance for larger deformations. Fig. 9 shows the evaluation results of SAFIRA without and with initialization by the proposed method for TOS and VSC applied to LBPA40 dataset with 10% and 20% deformation. Fig. 10 illustrates one sample result. Table 1 summarizes TOS and VSC score of three different registration approaches applied to LBPA40 dataset with 10% and 20% deformation.

Comparing Fig. 8 and 9 (a), it is observed that the proposed method has better performance for this data set. Fig. 10 (c) and (d) show sample results for proposed method and SAFIRA. The deformed image generated by the latter has lost some detail information which can be attributed to the re-gridding steps needed in the algorithm. Compare Fig. 9 (a) and (b), initialization by proposed method improves both TOS and VSC scores. The result of SAFIRA with our initialization in Fig. 10 (e) produces images very similar to the deformed image shown in column (b), which is better than pure SAFIRA shown in column (c).

Method	10%		20%	
	TOS	VSC	TOS	VSC
SAFIRA (40 iterations)	0.6313	0.1060	0.5396	0.1383
Proposed Method	0.8351	0.0516	0.7999	0.0701
SAFIRA with Initialization (40 iterations)	0.8340	0.0545	0.8671	0.0695

Table 1. TOS and VSC scores for three different registration approaches applied to LBPA40 dataset.

4. CONCLUSION

In this paper, a new non-rigid registration methodology is introduced which makes use of a Lipschitz deformation model in order to provide guarantees on the registration results. The uncertainty on the estimated deformation is derived from the size of feasible matching sets that are computed for individual point matches. Experiments using the LPBA40 dataset show that our method can estimate deformations with high-accuracy.

The results from our technique can be further refined by using them as an initialization to other approaches such as fluid or elastic registration methods. In the future, we aim to extend our approach to provide not only a single estimated map with large uncertainty, but also a few candidate maps with lower uncertainty, in order to provide more refined outcomes. Furthermore, the implementation will be extended to 3D imaging modalities in order to make it applicable to many other scenarios.

5. ACKNOWLEGEMENT

We would like to thank Dr. Natasha Lepore from University of Southern California and Dr. Helene Nadeau from Dawson College for providing us the SAFIRA code and information to run the code for comparison.

REFERENCES

[1] Maintz, J. and Viergever, M. A., "A survey of medical image registration," *Medical image analysis* **2**(1), 1–36 (1998).
[2] Maes, F., Collignon, A., Vandermeulen, D., Marchal, G., and Suetens, P., "Multimodality image registration by maximization of mutual information," *Medical Imaging, IEEE Transactions on* **16**, 187–198 (April 1997).
[3] Collignon, A., Maes, F., Delaere, D., Vandermeulen, D., Suetens, P., and Marchal, G., "Automated multi-modality image registration based on information theory," *Information processing in medical imaging* **3**, 263–274 (1995).
[4] Rueckert, D., Clarkson, M. J., Hill, D. L. G., and Hawkes, D. J., "Non-rigid registration using higher-order mutual information," *Medical Imaging 2000: Image Processing* **3979**, 438–447 (2000).
[5] Brun, C., Lepore, N., Pennec, X., Chou, Y.-Y., Lee, A., de Zubicaray, G., McMahon, K., Wright, M., Gee, J., and Thompson, P., "A nonconservative lagrangian framework for statistical fluid registration - safira," *Medical Imaging, IEEE Transactions on* **30**, 184–202 (Feb 2011).
[6] Zhang, J., Wang, J., Wang, X., and Feng, D., "The adaptive fem elastic model for medical image registration," *Physics in medicine and biology* **59**(1), 97 (2014).
[7] Roche, A., Pennec, X., Malandain, G., and Ayache, N., "Rigid registration of 3-d ultrasound with mr images: a new approach combining intensity and gradient information," *Medical Imaging, IEEE Transactions on* **20**, 1038–1049 (Oct 2001).
[8] Ourselin, S., Roche, A., Prima, S., and Ayache, N., "Block matching: A general framework to improve robustness of rigid registration of medical images," in [*Medical Image Computing and Computer-Assisted Intervention MICCAI 2000*], Delp, S., DiGoia, A., and Jaramaz, B., eds., *Lecture Notes in Computer Science* **1935**, 557–566, Springer Berlin Heidelberg (2000).
[9] Schnabel, J., Rueckert, D., Quist, M., Blackall, J., Castellano-Smith, A., Hartkens, T., Penney, G., Hall, W., Liu, H., Truwit, C., Gerritsen, F., Hill, D., and Hawkes, D., "A generic framework for non-rigid registration based on non-uniform multi-level free-form deformations," in [*Medical Image Computing and Computer-Assisted Intervention MICCAI 2001*], Niessen, W. and Viergever, M., eds., *Lecture Notes in Computer Science* **2208**, 573–581, Springer Berlin Heidelberg (2001).
[10] Bhatia, K. K., Hajnal, J. V., Puri, B. K., Edwards, A. D., and Rueckert, D., "Consistent groupwise non-rigid registration for atlas construction," in [*Biomedical Imaging: Nano to Macro, 2004. IEEE International Symposium on*], 908–911 Vol. 1 (April 2004).
[11] Moghe, A. A. and Singhai, J., "Article: Image registration: A review of elastic registration methods applied to medical imaging," *International Journal of Computer Applications* **70**, 6–11 (May 2013). Published by Foundation of Computer Science, New York, USA.
[12] Klein, S., Staring, M., Murphy, K., Viergever, M., and Pluim, J. P. W., "elastix: A toolbox for intensity-based medical image registration," *Medical Imaging, IEEE Transactions on* **29**, 196–205 (Jan 2010).
[13] Jenkinson, M. and Smith, S., "A global optimisation method for robust affine registration of brain images," *Medical Image Analysis* **5**(2), 143 – 156 (2001).
[14] Jenkinson, M., Bannister, P., Brady, M., and Smith, S., "Improved optimization for the robust and accurate linear registration and motion correction of brain images," *NeuroImage* **17**(2), 825 – 841 (2002).
[15] Berg, M., [*Computational geometry: algorithms and applications*], Springer, 3rd ed. (Mar. 2008).
[16] Zitov, B. and Flusser, J., "Image registration methods: a survey," *Image and Vision Computing* **21**, 977–1000 (2003).
[17] Klein, A., Andersson, J., Ardekani, B. A., Ashburner, J., Avants, B., and et al., "Evaluation of 14 nonlinear deformation algorithms applied to human brain mri registration," *NeuroImage* **46**(3), 786 – 802 (2009).